AIAA JOURNAL
Vol. 34, No. 1, January 1996

Measurements of the Triple Shock Wave/Turbulent Boundary-Layer Interaction

T. J. Garrison*
Louisiana State University, Baton Rouge, Louisiana 70803
G. S. Settles†
Pennsylvania State University, University Park, Pennsylvania 16802
and
C. C. Horstman‡
NASA Ames Research Center, Moffett Field, California 94035

A joint experimental and computational study has investigated the flowfield structure created by three crossing oblique shock waves interacting with a turbulent boundary layer. Such an interaction is of practical importance in the design of high-speed sidewall-compression inlets. The interaction is created by a test model consisting of two vertical sharp fins mounted at 15-deg angle of attack to a horizontal flat plate. A third compression surface of 10-deg angle is mounted to the plate between the two vertical fins. The Mach 3.85 flowfield is examined experimentally through kerosene lampblack and planar laser scattering visualizations. The results are used to develop a flowfield model of the interaction structure. This structure is found to consist of a complex wave pattern overlying a viscous separated region. The presence of the 10-deg compression ramp reduces the severity of the boundary-layer separation compared to interactions created by the two fins alone. Additionally, the experimental flowfield data are compared with a computational solution using a modified κ–ϵ (Rodi) turbulence model. A comparison of the results shows that, despite the complexity of the flowfield, the computed solution does reveal several of the key flow features observed experimentally.

Introduction

OVER the past several years there has been an ongoing research effort to understand the flowfield created by two crossing oblique shock waves interacting with a turbulent boundary layer. A major objective for studying this flowfield is to gain a basic understanding of the viscous/inviscid interactions within a generic high-speed sidewall-compression inlet. A great deal has been learned about this interaction through a range of experimental[1–15] and computational[16–22] investigations. The most prominent feature of the crossing-shock interaction is the large separated flow region it produces on the interaction centerline (cf., Refs. 9 and 14).

Of course, practical inlets likely involve more than just sidewall compression. Given the knowledge base formed by these crossing-shock studies, it is now possible to add additional features to the generic inlet.

This paper addresses the flowfield generated by adding a compression ramp to the existing crossing-shock model. The model geometry used to generate this interaction is shown in Fig. 1. In this geometry, a third compression surface is added to the generic inlet, making it more characteristic of realistic inlet designs.

There are two primary objectives of the present paper. The first is to present the experimentally obtained flow visualization results of the triple-shock interaction along with a discussion of the main flowfield features. The second objective is to compare the experimental results with a recently completed computational prediction of the triple-shock flowfield. Such a comparison is useful to assess the capabilities of current computational fluid dynamics (CFD) codes as well as to provide additional insight into the triple-shock interaction.

The joint experimental and computational results describedherein represent the first known investigation of the triple-shock flowfield. Because no experimental or computational data of any kind have been available on this interaction, the following results give valuable insight into the nature of the flow and provide a framework for further studies.

Description of Experiments

Wind-Tunnel Facility and Test Conditions

The experiments were performed in the Pennsylvania State Gas Dynamics Laboratory's Supersonic Wind Tunnel Facility, which is an intermittent blowdown tunnel with a test section size of 15 × 17 × 60 cm. The experiments described in this paper were carried out at a Mach number of 3.85, with a stagnation pressure of 1500 kPa, a stagnation temperature of 295 K, and a unit Reynolds number of 76×10^6/m. Typical run times of 45 s were achieved at these conditions.

Test Model

Figure 1 shows the model geometry used for the triple-shock experiments. This model consists of a compression ramp of angle $\phi = 10$ deg located between two vertical fins, both at angle of attack $\alpha = 15$ deg. Both the fins and the compression ramp are mounted to a horizontal flat plate with their leading edges coincident. The

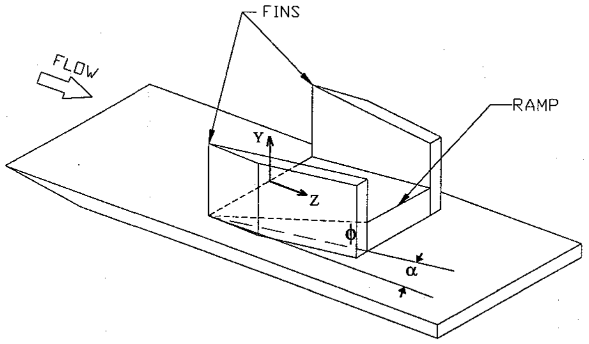

Fig. 1 Experimental triple-shock model.

Presented as Paper 94-2274 at the AIAA 25th Fluid Dynamics Conference, Colorado Springs, CO, June 20–23, 1994; received July 6, 1994; revision received March 13, 1995; accepted for publication March 17, 1995.

*Assistant Professor, Mechanical Engineering Department. Member AIAA.

†Professor, Mechanical Engineering Department, and Director, Gas Dynamics Laboratory. Associate Fellow AIAA.

‡Senior Scientist. Associate Fellow AIAA.

flat plate generates an equilibrium, nearly adiabatic, zero-pressure-gradient turbulent boundary layer that interacts with the three crossing oblique shock waves generated by the fins and ramp. The incoming properties of the boundary layer at the fin leading edge location are δ=3.5 mm, $\delta^* = 1.12$ mm, and $\theta = 0.13$ mm. Further details are reported in Ref. 14. The leading edges of the fins and ramp are located 21.3 cm downstream of the plate leading edge, with a transverse distance between the fin leading edges of 9.63 cm. The height of the fins is 8.25 cm. For the measurements described herein, a symmetric interaction about the plane $X = 0$ was produced.

Kerosene Lampblack Surface Traces

Limiting surface streamline patterns were recorded for the triple-shock interaction by applying a mixture of kerosene and lampblack to the flat plate and fin leading edges. The kerosene evaporates shortly after the pattern has formed, leaving the lampblack pigment on the surface. This lampblack pattern is then removed from the model surfaces using large squares of matte adhesive tape. The tape containing the surface pattern is then reapplied to a sheet of white paper, permanently preserving the pattern.

Planar Laser Scattering Visualization

Planar laser scattering (PLS), also known as laser light-screen or vapor-screen visualization, was used to record details of the entire interaction structure nonintrusively. This technique makes use of the slight amount of moisture present in the wind-tunnel air supply which freezes into submicron-sized particles during the nozzle expansion process. These ice particles interact with the laser light sheet, scattering the light with intensity related to the flow density. The scattered light is recorded by a charge-coupled device (CCD) camera and the images are stored on VHS videotape.

For the current PLS experiments, a 4 W argon-ion laser was used as the light source, with the beam formed into a thin sheet approximately 1 mm thick using a combination of spherical and cylindrical lenses. The light sheet was brought into the test section through an acrylic window in the ceiling of the wind tunnel. The sheet was oriented perpendicular to both the flat plate and freestream, and parallel to a line joining the fin tips.

A miniature CCD camera with a diameter of 17 mm (Panasonic model GP-MS112) was mounted in a sting located in the diffuser section of the wind tunnel to record the light sheet images. This setup provided a view along the centerline of the interaction, normal to the laser light sheet. In addition, both the light sheet optics and the camera sting assembly were mounted to Velmex linear drives with identical stepper motors. During the course of a run, both the light sheet and the camera were traversed in tandem, with the light sheet sweeping out the volume from the fin tips to the trailing edges. By continuously storing the light sheet images on VHS videotape, a tomographic view of the entire interaction region was recorded.

Description of Computation

The computation described in this paper solved the full three-dimensional mean compressible Reynolds-averaged Navier–Stokes equations in strong conservation form.[23] The computation, performed by Horstman, uses a modified κ–ε turbulence model[24] along with the hybrid numerical scheme of MacCormack.[25] The grid size for the computation is $40 \times 64 \times 79$ in the X, Y, and Z directions, respectively. This grid size was selected based on previous grid resolution studies performed for three-dimensional shock wave/turbulent boundary-layer interactions at Mach 3 and Mach 8.3 (Ref. 19). The grid had variable spacing in all three directions, with grid points clustered near the model surfaces and near the inviscid shock intersection. Adjacent to the fin and model surfaces, the local sublayer grid is orthogonal to the boundaries. Typical details on the grid can be obtained from Ref. 19.

The computational geometry was set to match that of the experiment. Because of the symmetry of the triple-shock interaction, however, the computation solves only half of the experimental domain. The boundary conditions for the computation are as follows. 1) On the inflow boundary, an incoming two-dimensional equilibrium turbulent boundary-layer profile is prescribed to match the experiment. 2) On the fin and compression ramp surfaces, the velocity vector and normal gradient of static pressure are set to zero. The wall temperature is set to 1.06 T_{aw} to match the average experimental value. 3) On the plane of symmetry, the normal component of velocity is set to zero, as are the normal gradients of static pressure, temperature, and the remaining two velocity components. 4) On the top and outflow boundaries, the gradient of all flow variables is set to zero. The computation was performed on a Cray Y-MP (single processor) and required over 30 h of CPU time.

Corner Flow Structure

The symmetric crossing-shock interaction is comprised of the confluence of two separate single-fin interactions. In previous analyses of this flowfield,[9] it was found that the symmetry plane could be used effectively to study the wave structure within the interaction. If the Y–Z plane of symmetry along the interaction centerline is an inviscid reflection plane or inviscid "wall," waves that intersect this plane must be ideally reflected (since there is no boundary layer present). Such a situation must occur to maintain the interaction symmetry and to satisfy continuity. With this interpretation, the symmetric crossing-shock interaction was previously analyzed in terms of the reflection of a single-fin interaction from an inviscid wall.[8–10,14]

Because the triple-shock interaction shown in Fig. 1 is also symmetric, the same reflection-plane analysis can be used to understand its structure. Whereas the crossing-shock interaction was treated as the reflection of a single-fin interaction, the triple-shock interaction can be thought of as the reflection of a corner flow interaction. Thus, it is important to understand the structure of the corner flow which undergoes the reflection process. The remainder of this section reviews the main features of the corner flow which makes up the triple-shock interaction.

The supersonic flowfield created in the corner of two intersecting wedges has received a great deal of study over the past several decades. Charwat and Redekeopp[26] were the first to develop a flowfield model of the inviscid wave structure in a corner. Numerous additional investigations have been performed for a range of incoming Mach numbers and wedge angles. Because past studies did not addresses the particular Mach number and wedge angle combination of interest to the present investigation, however, PLS visualizations of the corner flow were performed as part of the current study.

Figure 2 shows a PLS image for a corner flow created by a 15-deg fin and a 10-deg ramp in a Mach 3.85 freestream flow. This image, taken 11.1 cm from the combined fin and ramp leading edge, shows the shock wave structure in a plane normal to the freestream flow direction (i.e., an X–Y plane). Figure 3 shows a schematic of the flowfield features revealed in the PLS image of Fig. 2. Qualitatively, the interaction structure shown in Figs. 2 and 3 is in good agreement with that of previous corner flow models.[27] The flowfield within the corner consists of the inviscid shocks generated by the fin and ramp joined by a corner shock. This corner shock is the result of an irregular (i.e., Mach) intersection of the two inviscid shocks. Also, emanating from the ends of the corner shock are two embedded shock waves. These embedded shocks both bifurcate into a separation and rear shock due to their interactions with the fin and ramp

Fig. 2 PLS image of corner flow interaction, $M_\infty = 3.85$, $\phi = 10$ deg, $\alpha = 15$ deg.

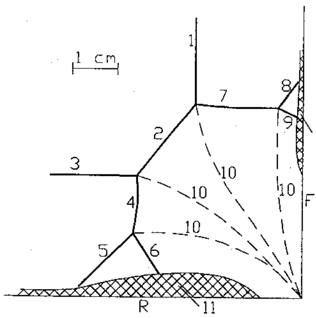

Fig. 3 Flowfield diagram for Fig. 2, with *R* ramp, *F* fin; shocks: 1 fin inviscid, 2 corner, 3 ramp inviscid, 4 fin embedded, 5 fin separation, 6 fin rear, 7 ramp embedded, 8 ramp separation, 9 ramp rear; other: 10 slipline, and 11 separated region.

boundary layers. In future discussions it will be useful to distinguish between these two embedded shock systems. Thus, they have been identified in Fig. 3 based on whether they are generated by the fin or ramp surface. Beneath the two bifurcated shock systems are two separated flow regions.

Additionally, within the corner interaction there are four triple points and four corresponding sliplines. All of the sliplines asymptote together and terminate at the ramp–fin intersection.

As already stated, the triple-shock interaction can be considered as the reflection of this corner flow. However, it should be noted that insofar as the structure of the corner flow is already complex its reflection can be expected to be still more complex in structure.

Results

Triple-Shock Limiting Streamline Pattern

Figure 4a shows a kerosene-lampblack surface flow visualization for the triple-shock interaction. An annotated tracing of this pattern is given in Fig. 4b for clarity. Upstream, near the fin and ramp leading edges, the surface pattern near each fin is identical to that of a corner-flow interaction.[27] The prominent features in the surface pattern include the upstream influence line (UI), the primary attachment line (PA), and the primary separation line (PS). The location of the inviscid fin shock (IFS) is also shown for reference. In the upstream portion of the flow, the surface features appear as straight lines due to the conical nature of the corner flow. These features remain as straight conical rays until the point at which the two upstream influence lines meet, whence the various lines begin to deviate significantly from conical behavior. This point marks the location at which the two corner flows begin to sense the presence of one another.

Following the primary separation lines (PS) farther downstream in Fig. 4b, they are observed to initially converge toward the interaction centerline and then diverge from it. Upon reaching a local maximum distance from the centerline, the separation lines again converge slowly toward it. This same converging-diverging-converging separation-line pattern was observed previously in surface traces of crossing-shock interactions[9,10] such as the one shown in Fig. 5. The trace shown in Fig. 5 is for the same fin angles (15-deg) and incoming Mach number (3.85) as the triple-shock trace shown in Fig. 4a.

In Fig. 4a, near the interaction centerline, between the two primary separation lines, the surface streamlines diverge from the centerline and converge upon the separation lines on either side, indicating a line of flow attachment on the interaction centerline. Again, this same behavior has been observed in studies of crossing-shock interactions.

It is useful to compare in more detail the triple-shock trace shown in Fig. 4 to the corresponding crossing-shock trace of Fig. 5. Although the basic features of these patterns are similar, it is clear that details in the vicinity of the interaction centerline are distinctly different. The most interesting aspect of the comparison is that the spanwise extent of the surface features near the centerline is much smaller in the triple-shock interaction. In fact, the surface pattern for the triple-shock interaction is very similar to that of a weaker, Mach 3, $\alpha = 11$-deg crossing-shock interaction.[10,14] Because it has been shown that the topological features near the interaction centerline are associated with the separation of the incoming boundary layer,[10] it appears that the separation caused by the triple-shock interaction is less severe than that caused by the crossing-shock interaction of equal fin angles, despite the fact that the overall compression is greater in the triple-shock configuration. This observation is very important, since the major problem identified with using the crossing-shock configuration as a high-speed inlet is its large separated region. This topic is discussed further in the following section.

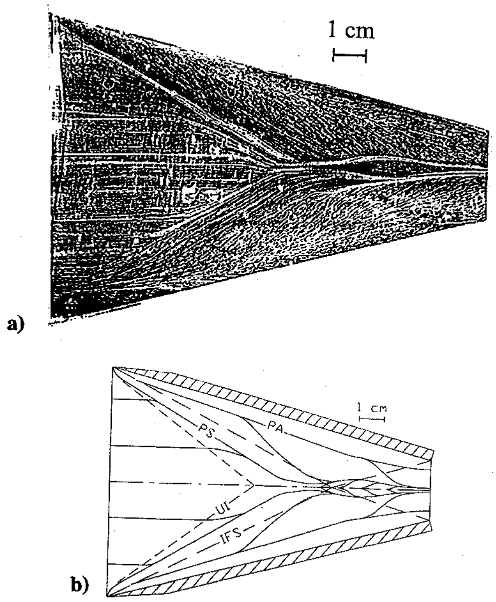

Fig. 4 Experimental surface flow pattern: a) actual trace and b) sketch showing key features.

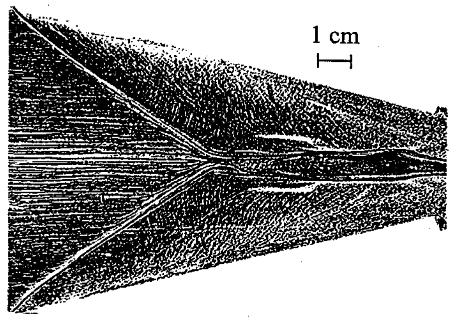

Fig. 5 Trace for $M_\infty = 3.85$, $\alpha = 15$-deg crossing-shock interaction.

It is also useful to compare the experimental triple-shock surface flow pattern to that predicted by the computation, shown in Fig. 6. A comparison of Figs. 4 and 6 shows that, upstream, near the fin and ramp leading edges, the patterns are similar. Moving downstream, however, differences in the patterns become evident, especially in the vicinity of the interaction centerline. In the computation, the primary separation lines asymptote upon the interaction centerline, failing to exhibit the converging-diverging-converging pattern seen in the experiment. Similar discrepancies between experimental and computed surface flow patterns in the vicinity of the interaction centerline were also observed in previous crossing-shock studies.[7,9,15] The most likely reason for such errors is believed to be the inadequacy of the turbulence model used.

Nonetheless, it is interesting to note that a comparison of the computed triple-shock pattern shown in Fig. 6 to a previously computed pattern for the crossing-shock interaction of the same fin angles[14] reveals a significant reduction in the size of the topological features near centerline in the former case. This is the same observation made in the comparison of the experimental traces discussed earlier. In fact, the computed shear stress along the centerline of the triple-shock interaction is everywhere greater than zero, unlike the crossing-shock interaction in which both the experimental and computed shear stress goes to zero on centerline.[7]

Experimental Flowfield Structure

A sequence of eight PLS images of the triple-shock interaction is next given in Fig. 7. These PLS images can be used to determine

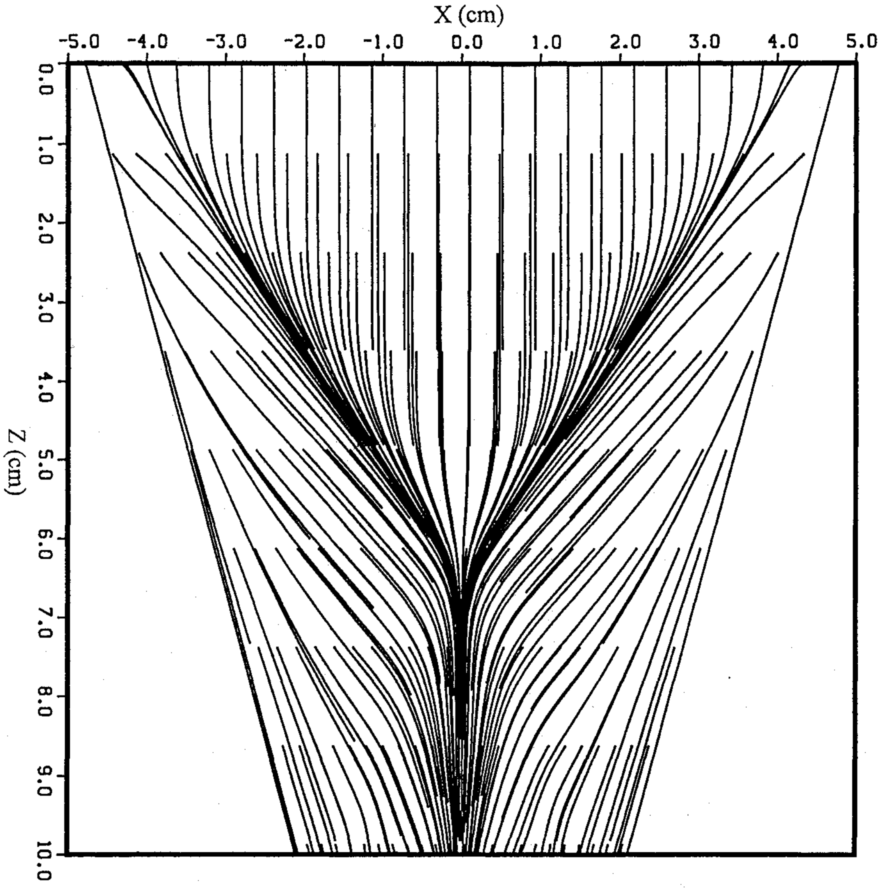

Fig. 6 Computed triple-shock surface trace.

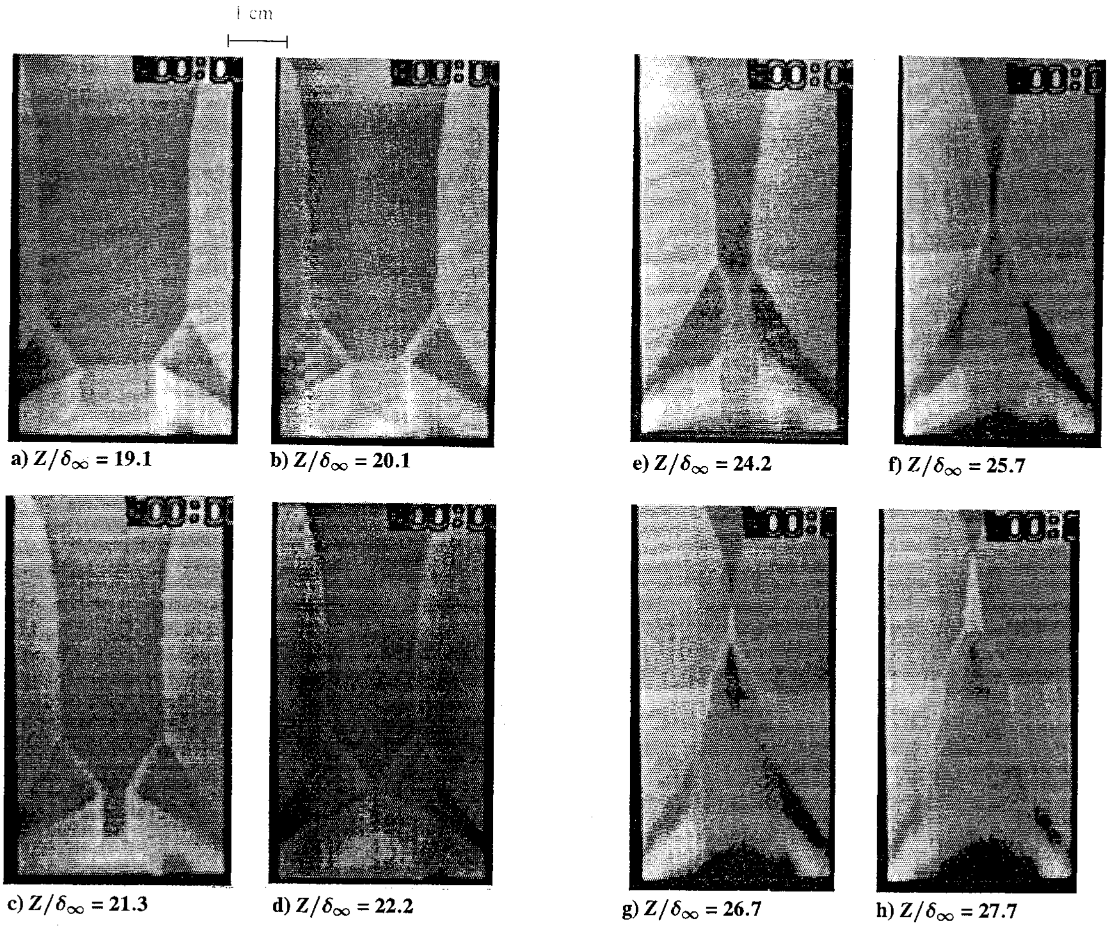

a) $Z/\delta_\infty = 19.1$

b) $Z/\delta_\infty = 20.1$

e) $Z/\delta_\infty = 24.2$

f) $Z/\delta_\infty = 25.7$

c) $Z/\delta_\infty = 21.3$

d) $Z/\delta_\infty = 22.2$

g) $Z/\delta_\infty = 26.7$

h) $Z/\delta_\infty = 27.7$

Fig. 7 PLS images for a $M_\infty = 3.85$, $\alpha = 15$ deg, $\phi = 10$-deg triple-shock interaction.

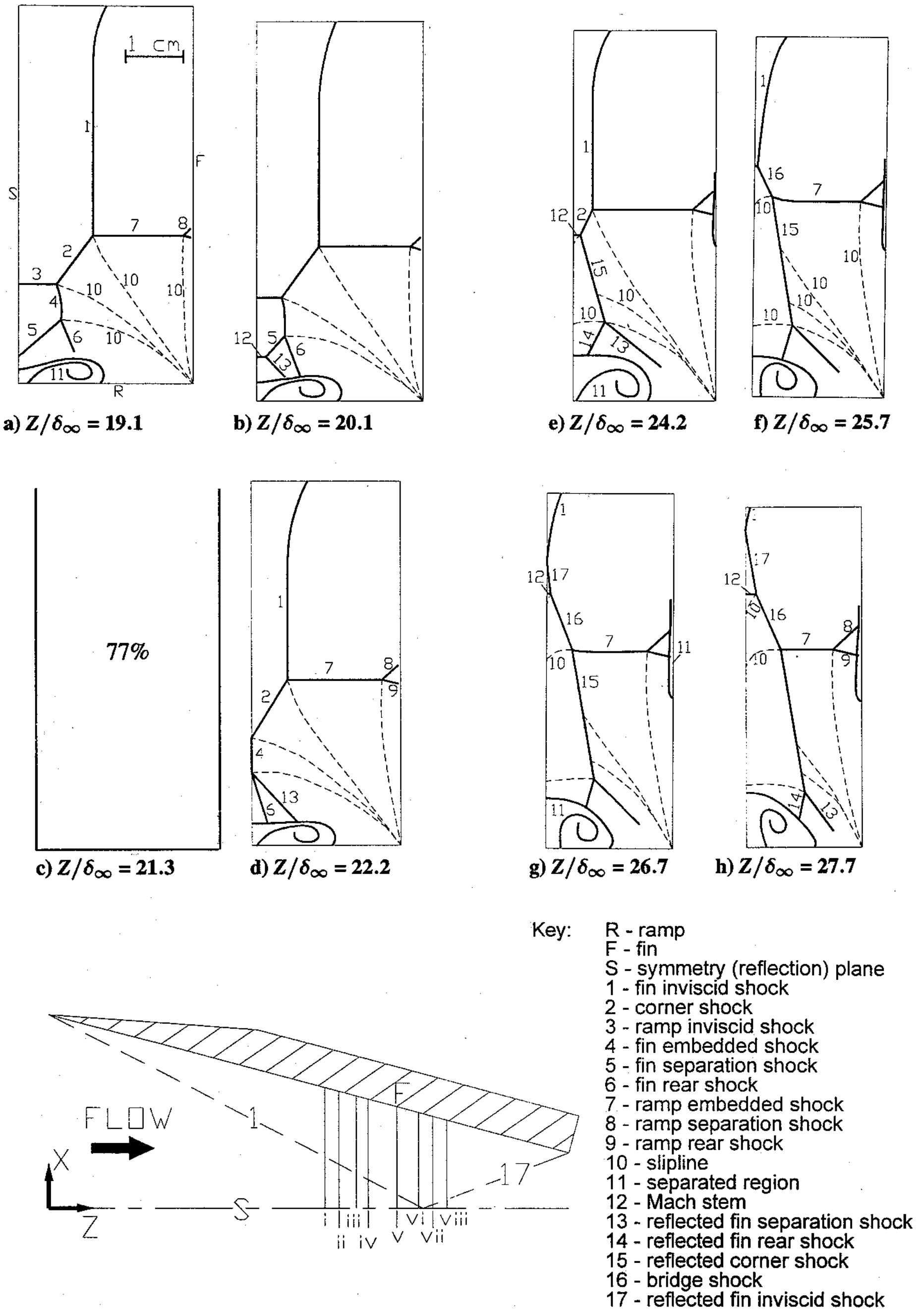
a) $Z/\delta_\infty = 19.1$ b) $Z/\delta_\infty = 20.1$ e) $Z/\delta_\infty = 24.2$ f) $Z/\delta_\infty = 25.7$

c) $Z/\delta_\infty = 21.3$ d) $Z/\delta_\infty = 22.2$ g) $Z/\delta_\infty = 26.7$ h) $Z/\delta_\infty = 27.7$

Fig. 8 Flowfield diagrams corresponding to Fig. 7 for a Mach 3.85, α = 15 deg, ϕ = 10-deg triple-shock interaction.

the location of the shock waves and sliplines within the flow as well as the size and shape of the separated flow regions. In the images of Fig. 7, shock waves and sliplines appear as distinct intensity jumps. The boundary-layer and separated flow regions appear dark in the PLS images due to extinction of the ice particles caused by the elevated temperatures within these viscous regions.

Figure 8 shows a corresponding interpretation of the features of the PLS imagery of Fig. 7. The images in Fig. 8 are shown for an observer located downstream of the interaction. Based on the symmetry of the interaction, however, only its right-half is shown in Fig. 8. Further, although the camera field of view for the images of Fig. 7 is partially obscured by both fins and the ramp, the missing detail near the model surfaces has been furnished in Fig. 8 based on extrapolation and some interpolation of the images shown in Fig. 7. It should also be noted that the intent of the flowfield model shown in Fig. 8 is to identify the major features within the flowfield. The complexity of the triple-shock interaction and the limited resolution of the PLS images preclude resolving many of the more intricate flow details (e.g., slight shock curvatures, weak shocks, and complex shock intersections).

The streamwise location of each frame of Figs. 7 and 8 is noted below the image. For reference, the oblique shock waves created by the fins cross at $Z = 92$ mm or $Z/\delta_\infty = 26.3$. A top view of the interaction showing the locations of the eight PLS planes is given in Fig. 8 for clarity.

In Figs. 7a and 8a the flowfield features are the same as those of two separate corner flow interactions, shown earlier in Fig. 3. As mentioned earlier, to understand the confluence of these two corner flows, it is useful to consider the Y–Z plane along the interaction centerline as an inviscid reflection plane. In this way, the analysis of the triple-shock flow is treated as the reflection of a single corner flow interaction from an inviscid wall.

Figures 7b and 8b occur slightly downstream of the location where the two fin separation shocks meet. Using the reflection plane analogy, it can be seen that the incident fin separation shock (5) reflects from this plane, appearing as a bright region in the PLS images on the interaction centerline near the plate surface. (The numbers in parentheses refer to the diagrams of Fig. 8.) Although hard to detect in the still images of Fig. 7, the videotape shows that the reflection of the fin separation shock is an irregular or Mach reflection. It is interesting to note that the reflection of the embedded fin shock system is exactly analogous to the reflection process which occurs in a crossing-shock interaction.[9] Thus, near the ramp surface, the triple-shock interaction contains an embedded crossing-shock interaction. It is therefore no surprise that the surface flow patterns of Figs. 4a and 5 are similar in all respects except the strength of the interaction.

The Mach reflection of the fin separation shock continues in Figs. 7c and 8c. Additionally, as the embedded fin separation shock reflects in Figs. 7a–7c and 8a–8c, the width of the ramp shock (3) decreases continuously. By Figs. 7d and 8d the ramp shock ceases to exist and the corner shock (2) just intersects the reflection plane. Figures 7d and 8d also mark the location at which the fin separation shock reflection is complete and the fin embedded shock (4) and rear shock (6) strike the reflection plane.

The reflection of the corner shock (2), which began at Figs. 7d and 8d, continues in Figs. 7e and 8e and is complete prior to Figs. 7f and 8f. As with the fin separation shock, the corner shock also appears to undergo a Mach reflection, resulting in the formation of the Mach stem (12) shown in Figs. 7e and 8e. Just before Figs. 7f and 8f, the three-shock intersection or "triple point" joining the corner shock, ramp embedded shock, and inviscid fin shock strikes the reflection plane. It is observed that the reflection of this triple point is also irregular and produces two additional shock segments. The new shock segments, a Mach stem (12) and a "bridge" shock (16), are labeled in Fig. 8g. A similar situation was observed to occur for a triple-point reflection in the crossing-shock flowfield studied earlier.[9]

It is important to note that by Figs. 7g and 8g the interaction wave structure has propagated a significant distance away from the ramp surface. Unlike the case in Figs. 8a–8f, in Fig. 8g and beyond there is no longer a straight segment of inviscid fin shock (1). The curvature of this wave is due to the finite height of the fin which generates it. Thus, for Fig. 8g and beyond the fin height influences the interaction and renders it no longer semi-infinite. The curvature of the inviscid fin shock gives rise to a more complex reflected inviscid wave.

Figures 7g and 8g mark the approximate streamwise location at which the reflection of the incident corner flow from the reflection plane is complete. (The inviscid fin shocks continue to reflect due to their curvature.) The reflected wave system then propagates out toward the fin surface, as shown in Figs. 7h and 8h. Provided the fins are long enough, another sequence of reflections will occur at the fin surface with the added complexity of viscous effects associated with the fin boundary layer. We have made no attempt to model that occurrence here.

In addition to the wave structure just described, it is also of interest to follow the evolution of the sliplines and separated flow regions. As the corner flow shock structure propagates toward the reflection plane, the sliplines originating at the four triple points extend into the fin-ramp junction. However, it is observed that, once a given triple point reflects from the reflection plane, its corresponding slipline then grows outward from the interaction centerline (cf., Figs. 7g and 8g). The sliplines originally created during propagation toward the centerline appear to be "washed-out" as the wave structure propagates back toward the fin.

Through much of the upstream portion of the interaction, the separated flow regions on the fin and ramp surfaces are obscured in the PLS images of Fig. 7. The top of the separated region on the ramp is first visible in Fig. 7e of the PLS images, whereas the separated regions on the fin surfaces remain outside the camera field of view in all of the figures. Thus, the size and location of the fin separated region shown in Fig. 8 are approximate. The separated regions on the fins are very small and are located close to the surface. This is a result of the extremely thin boundary layer on the fins compared to that on the ramp. (The ramp boundary layer originates at the leading edge of the flat plate, 21.3 cm ahead of the fin leading edges.) Also, the ramp embedded shock wave which interacts with the fin boundary layer is weaker due to the 10-deg deflection angle of the ramp compared to the 15-deg fin angle.

Figure 9 shows a PLS image taken at the trailing edge of the fins and ramp. Although the wave structure is difficult to see at this plane, the image shows the size and shape of the separated region on the ramp surface. It is useful to compare this image (on the left) with an image taken at the same location without the ramp in place (i.e., for a crossing-shock interaction) as shown on the right half of Fig. 9. The two images in Fig. 9 are to the same scale, although the crossing-shock image has been shifted vertically to align the locations of the horizontal model surfaces.

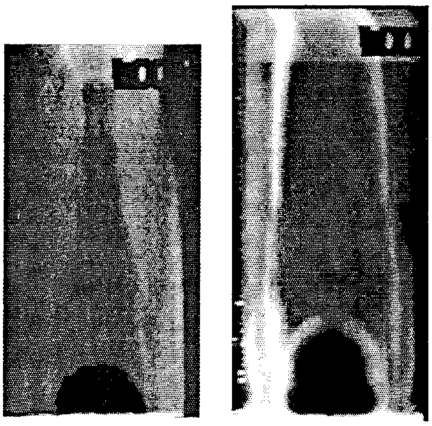

Fig. 9 PLS images at Z/δ_∞ = 36.3 for triple-shock (left) and crossing-shock (right) interactions.

Figure 9 clearly shows that the size of the separated flow region is significantly smaller in the triple-shock interaction, despite the fact that the overall compression is greater for this configuration. This result is consistent with that observed in the preceding analysis of the surface flow pattern. Comparing the areas of the separated regions in Fig. 9 shows that the triple-shock separated flow region is approximately 45% smaller than that of the crossing-shock flow. Comparing the size of the separated flow region normalized by the exit area shows the triple-shock separated region occupies 25% less of the exit area than that of the crossing-shock flow.

It is important to understand why the added compression surface in the triple-shock geometry reduces the severity of the boundary-layer separation over that without the compression ramp. In the triple-shock case, provided the ramp angle is less than that required for incipient separation, the compression ramp is able to "precompress" the incoming boundary layer without causing it to separate. (For a compression ramp at Mach 3.85, incipient turbulent boundary-layer separation occurs at a ramp angle of $\phi \approx 20$ deg.) Because the Mach number is reduced through the ramp shock, the strength of the interaction caused by the fin shocks is also reduced compared to the case without the ramp. Thus, in the triple-shock interaction the fin separation and rear shocks are significantly weaker than those of the corresponding crossing-shock interaction, hence, the size of the separated region beneath these waves is significantly smaller. In effect, although the triple-shock configuration adds more compression, this compression is distributed in such a way as to reduce the potential for boundary-layer separation. This observation suggests that modifications to the crossing-shock geometry might be made to reduce the extent of the separated region and increase the overall inlet compression. It also demonstrates that higher overall inlet compression does not necessarily increase the severity of boundary-layer separation.

Comparison with Computed Results

The remainder of this section compares the earlier described experimental flowfield to that obtained from the computation. For brevity, the experiment and computation are compared only at two planes within the interaction. Similar results are found throughout the entire interaction.

Figure 10 shows the computed static pressure distribution at $Z/\delta_\infty = 20.1$ (left) and 25.7, which corresponds to the location of Figs. 7b and 7f. For comparison, the experimental flowfield model from Fig. 8 has been overlaid on the computed pressure distribution. Overall, there is relatively good agreement between the computation and experiment in the outer inviscid region, with the computed pressure contours reasonably matching the experimental wave locations within the resolution of the former. However, unlike the

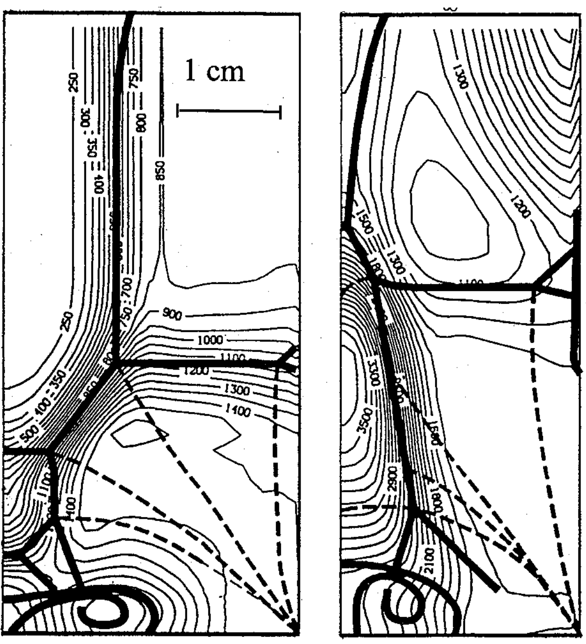

Fig. 10 **Comparison of the computed static pressure contours (kPa) with the experimental flowfield model at $Z/\delta_\infty = 20.1$ (left) and 25.7 (right).**

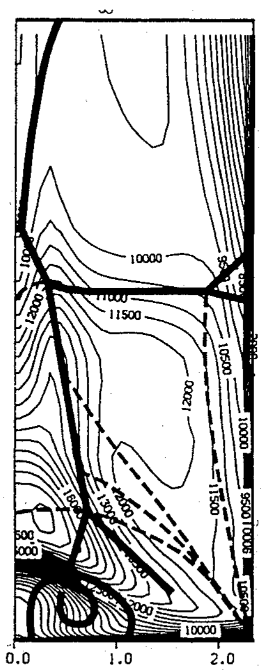

Fig. 11 **Comparison of the computed pitot pressure contours (kPa) with the experimental flowfield model at $Z/\delta_\infty = 25.7$.**

experimental PLS images, the shock waves in the computation are poorly captured, the pressure rise across these waves being spread out over a significant distance.

The fact that the computation is able to reasonably predict the flowfield structure at the downstream location is notable. As shown in the left plot of Fig. 10, the resolution of the computed incident corner flow is very coarse. In such a case, it is unclear that the physics of complex wave reflections will be captured by the computation. One possibility is that poor resolution might lead to a distinctly nonphysical downstream flow pattern. However, at least in the present example, such an error does not occur.

The computed static pressure contours of Fig. 10 do not reveal the separated flow region on the ramp surface, which is observed in the experiment. The contours of the computed pitot pressure, however, shown in Fig. 11, do show its presence. The same result was seen in comparisons of the crossing-shock flow.[15] In that case, experimental static, stagnation, and pitot pressure contours obtained with a five-hole probe all revealed the presence of the separated region. The computations revealed the separated region only in the stagnation and pitot pressure, however, not the static pressure. For the crossing-shock flow described in Ref. 15, it was found that the computations were in significant error within the separated flow region. Because of the similarity, it is expected that the computed results within the separated region of the triple-shock interaction may also be in error. Further research is needed to address this issue in detail.

Finally, a comparison of the computed separated region shown in Fig. 11 to that previously computed[14] for a crossing-shock interaction shows that the triple-shock geometry produces a significantly smaller separated flow region. This result is consistent with that seen in the experimental results of Fig. 9.

Hence, despite its limitations, the computation does provide valuable insight into the flow structure. It predicts the separation and subsequent accumulation of the incoming boundary layer on centerline and the crude shock wave structure. It also shows that the size of the separated region is smaller than for the corresponding crossing-shock flow.

Conclusions

The flowfield structure of a symmetric triple-shock/turbulent boundary-layer interaction has been examined both experimentally and computationally for the first time. The nature of the shock wave structure and viscous region were studied. The following overall conclusions and observations have been reached. 1) The triple-shock interaction represents the confluence of two conical corner flows, from which a complex, fully three-dimensional, viscous/inviscid interaction develops. 2) By treating the symmetry plane as an inviscid reflection plane and analyzing the reflection of a corner-flow interaction, the flowfield structure of the triple-shock interaction is revealed. 3) Results of this reflection-plane analysis show that the shock structure comprises a complex reflection, resulting in the formation and elimination of various waves. The level of complexity of the flowfield goes well beyond that of the single-fin and crossing-shock interactions studied previously. 4) Although there is boundary-layer separation on the ramp, the extent of the separated region is significantly smaller than that produced in crossing-shock studies without the compression ramp. This result is important in the design of high-speed inlets. It shows that higher inlet compression does not necessarily lead to more serious boundary-layer separation. 5) Despite the complexity of the triple-shock interaction and low-grid resolution, the computation was able to predict the gross flowfield structure. This is significant, but does not mean that all computations with poor grid resolution will nonetheless capture the essence of the flow. To fully evaluate the computation's accuracy, additional experimental data are required both within the flowfield and on the model surface. Additional computations with finer grid resolutions would also be highly beneficial.

Acknowledgments

This work was sponsored by the Air Force Office of Scientific Research under Grant 89-0315, monitored by Len Sakell, and by NASA Ames Grant NGT-50952, monitored by C. C. Horstman.

References

[1] Mee, D. J., Stalker, R. J., and Stollery, J. L., "Glancing Interactions Between Single and Intersecting Oblique Shock Waves and a Turbulent Boundary Layer," *Journal of Fluid Mechanics*, Vol. 170, Sept. 1986, pp. 411–433.

[2] Batcho, P. F., Ketchum, A. C., Bogdonoff, S. M., and Fernando, E. M., "Preliminary Study of the Interactions Caused by Crossing Shock Waves and a Turbulent Boundary Layer," AIAA Paper 89-0359, Jan. 1989.

[3] Bogdonoff, S. M., and Poddar, K., "An Exploratory Study of a Three-Dimensional Shock Wave Turbulent Boundary Layer Interaction," AIAA Paper 91-0525, Jan. 1991.

[4] Hingst, W. R., and Williams, K. E., "Interaction of Two Glancing, Crossing Shock Waves with Turbulent Boundary Layers at Various Mach Numbers," NASA TM 103740, 1991.

[5] Bogdonoff, S. M., and Stokes, W. L., "Crossing Shock Wave Turbulent Boundary Layer Interactions—Variable Angle and Shock Generator Length Geometry Effects at Mach 3," AIAA Paper 92-0636, Jan. 1992.

[6] Poddar, K., and Bogdonoff, S. M., "A Study of the Unsteadiness of Crossing Shock Wave Turbulent Boundary Layer Interactions," AIAA Paper 90-1456, June 1990.

[7]Garrison, T. J., and Settles, G. S., "Laser Interferometer Skin-Friction Measurements of Crossing-Shock Wave/Turbulent Boundary-Layer Interactions," *AIAA Journal*, Vol. 32, No. 6, 1994, pp. 1234–1241.

[8]Garrison, T. J., and Settles, G. S., "Flowfield Visualization of Crossing Shock-Wave/Boundary Layer Interactions," AIAA Paper 92-0750, Jan. 1992.

[9]Garrison, T. J., Settles, G. S., Narayanswami, N., and Knight, D., "Structure of Crossing Shock-Wave/Turbulent Boundary Layer Interactions," *AIAA Journal*, Vol. 31, No. 12, 1993, pp. 2204–2211.

[10]Garrison, T. J., and Settles, G. S., "Interaction Strength and Model Geometry Effects on the Structure of Crossing-Shock Wave/Turbulent Boundary-Layer Interactions," AIAA Paper 93-0780, Jan. 1993.

[11]Kussoy, M. I., and Horstman, K. C., "Intersecting Shock-Wave/ Turbulent Boundary-Layer Interactions at Mach 8.3," NASA TM 103909, Feb. 1992.

[12]Kussoy, M. I., Horstman, K. C., and Horstman, C. C., "Hypersonic Crossing Shock-Wave/Turbulent-Boundary-Layer Interactions," AIAA Paper 93-0781, Jan. 1993.

[13]Forkey, J., Cogne, S., Smits, A., Bogdonoff, S., Lempert, W. R., and Miles, R. B., "Time-Sequenced and Spectrally Filtered Raylieigh Imaging of Shock Wave and Boundary Layer Structure for Inlet Characterization," AIAA Paper 93-2300, June 1993.

[14]Garrison, T. J., "The Interaction Between Crossing-Shock Waves and a Turbulent Boundary Layer," Ph.D. Thesis, Mechanical Engineering Dept., Pennsylvania State Univ., University Park, PA, Aug. 1994.

[15]Garrison, T. J., Settles, G. S., Narayanswami, N., Knight, D. D., and Horstman, C. C., "Comparison of Flowfield Surveys and Computations of a Crossing-Shock Wave/Boundary Layer Interaction," AIAA Paper 94-2273, June 1994.

[16]Gaitonde, D., and Knight, D. D., "Numerical Experiments on 3-D Shock Wave-Boundary Layer Interaction Generated by a Sharp Fin," AIAA Paper 88-0309, Jan. 1988.

[17]Reddy, D. R., "3-D Navier–Stokes Analysis of Crossing, Glancing Shocks/Turbulent Boundary Layer Interactions," AIAA Paper 91-1758, June 1991.

[18]Narayanswami, N., Knight, D., Bogdonoff, S. M., and Horstman, C. C., "Interaction Between Crossing Oblique Shocks and a Turbulent Boundary Layer," *AIAA Journal*, Vol. 30, No. 8, 1992, pp. 1945–1952.

[19]Narayanswami, N., Knight, D. D., and Horstman, C. C., "The Investigation of a Hypersonic 3-D Crossing Shock/Turbulent Boundary Layer Interaction," *Shock Waves*, Vol. 3, No. 1, 1993, pp. 35–48.

[20]Narayanswami, N., Horstman, C. C., and Knight, D. D., "Numerical Simulation of Crossing Shock/Turbulent Boundary Layer Interaction at Mach 8.3—Comparison of Zero- and Two-Equation Turbulence Models," AIAA Paper 93-0779, Jan. 1993.

[21]Narayanswami, N., Horstman, C. C., and Knight, D. D., "Computation of Crossing Shock/Turbulent Boundary Layer Interactions at Mach 8.3," *AIAA Journal*, Vol. 31, No. 8, 1993, pp. 1369–1376.

[22]Gaitonde, D., and Shang, J. S., "Calculations on a Double-Fin Turbulent Interaction at High Speed," AIAA Paper 93-3432, Aug. 1993.

[23]Rubesin, M., and Rose, W., "The Turbulent Mean Flow Reynolds-Stress and Heat Flux Equations in Mass Averaged Dependent Variables," NASA TMX 62248, March 1973.

[24]Rodi, W., "Experience with Two-Layer Models Combining the $\kappa-\varepsilon$ with a One-Equation Model Near the Wall," AIAA Paper 91-0216, Jan. 1991.

[25]MacCormack, R. W., "A Numerical Method for Solving the Equations of Compressible Viscous Flow," *AIAA Journal*, Vol. 20, No. 9, 1982, pp. 1275–1281.

[26]Charwat, A. F., and Redekeopp, L. G., "Supersonic Interference along the Corner of Intersecting Wedges," *AIAA Journal*, Vol. 5, No. 3, 1967, pp. 480–488.

[27]West, J. E., and Korkegi, R. H., "Supersonic Interaction in the Corner of Intersecting Wedges at High Reynolds Numbers," *AIAA Journal*, Vol. 10, No. 5, 1972, pp. 652–656.